Chemical Engineering Journal 515 (2025) 163227

Contents lists available at ScienceDirect

Chemical Engineering Journal

journal homepage: www.elsevier.com/locate/cej

# Folic acid-targeted macrophage membrane-coated carbon quantum dot nanoplatform for dual drug and gene delivery in metastatic osteosarcoma therapy

Enyang Yao [a,1], Yang Li [b,1], Kai Deng [c], Wei He [d,*], Milad Ashrafizadeh [e], João Conde [f,*], Liyu Yang [a,*]

[a] Department of Orthopedics, The Shengjing Hospital of China Medical University, Shenyang, Liaoning 110004, China
[b] Department of Obstetrics and Gynecology, The Shengjing Hospital of China Medical University, Shenyang, Liaoning 110004, China
[c] The Second Clinical College of China Medical University, No. 36 Sanhao Street, Heping District, Shenyang, Liaoning Province 110004, China
[d] Department of Thoracic Surgery, The Shengjing Hospital of China Medical University, Shenyang, Liaoning 110004, China
[e] Department of Radiation Oncology, Shandong Provincial Key Laboratory of Radiation Oncology, Shandong Cancer Hospital and Institute, Shandong First Medical University, Shandong Academy of Medical Sciences, Jinan, Shandong 250000, China
[f] Comprehensive Health Research Centre (CHRC), NOVA Medical School, Faculdade de Ciências Médicas, NMS|FCM, Universidade NOVA de Lisboa, Lisboa, Portugal

ARTICLE INFO

*Keywords:*
Osteosarcoma
Biomimetic
Carbon quantum dot
Zoledronic acid
INHBA
Camouflaged nanoparticles

ABSTRACT

Osteosarcoma is the most common primary bone tumor with a high metastatic rate. Despite the improvement in patient prognosis with conventional therapeutics, enhancing the survival of patients with metastatic disease remains a challenge. Zoledronic acid (ZOL) stimulates apoptosis in cancer cells and is considered a promising drug for osteosarcoma therapy. Moreover, depletion of Inhibin Subunit Beta A (INHBA), a member of the transforming growth factor superfamily, can suppress osteosarcoma cell proliferation and invasion. Regarding the restricted potential of monotherapy, combination therapies, such as small interfering RNA (siRNA) and chemotherapy, are ideal strategies. However, off-target effects and adverse impacts lead to unsatisfactory clinical efficacy of these drugs. To address this challenge, we designed a folic acid-modified macrophage membrane coated with a carbon quantum dot (CQD) nanoplatform for the co-delivery of ZOL and siINHBA (ZOL-siINHBA@CQD@RM-FA). The anticancer activity of this nanotherapeutic agent was examined *in vitro* and *in vivo*. ZOL-siINHBA@CQD@RM-FA was approximately 200.7 nm in size, had a negative charge, excellent pH responsiveness, desirable biocompatibility, and high cellular uptake. This nanosystem achieved favorable co-delivery of ZOL/siINHBA and impaired osteosarcoma proliferation and invasion *in vitro*. Notably, intravenous administration facilitated tumor growth regression and inhibited lung metastasis without systemic toxicity. Accordingly, this nanotherapy could be considered an effective treatment for osteosarcoma, and this nanodelivery system shows potential for combined therapy by co-delivering genes and chemotherapy drugs.

## 1. Introduction

Osteosarcoma is an aggressive and lethal tumor in children and adolescents that results from malignant osteoid development caused by mesenchymal bone-forming cells [1]. Currently, the standard therapeutics for osteosarcoma include extensive surgical resection, chemotherapy, and radiation (for patients deemed unsuitable for surgery). Adjuvant chemotherapy has been beneficial in improving the 5-year survival rate of patients by up to 65 % [2]. Although the use of chemotherapeutic agents can increase the 5-year survival rate of patients with osteosarcoma, it is limited to patients without metastasis. In the case of metastasis, the 5-year survival rate of patients with osteosarcoma decreases to 20 % [3]. However, metastasis can occur early in osteosarcoma, especially in the lungs, and once metastasis has occurred, the 5-year survival rate is significantly reduced [4]. To date, effective treatment options to disrupt the progression of osteosarcoma metastasis

* Corresponding authors at: Department of Orthopedics, The Shengjing Hospital of China Medical University, Sanhao Street 36, Heping District, Shenyang City, Liaoning 110004, China (L. Yang).
*E-mail addresses:* kevin1346790@163.com (W. He), joao.conde@nms.unl.pt (J. Conde), yanglycmu@126.com (L. Yang).
[1] These authors contributed equally to this work.

https://doi.org/10.1016/j.cej.2025.163227
Received 6 January 2025; Received in revised form 23 April 2025; Accepted 28 April 2025
Available online 30 April 2025

have not been developed, and the prognosis of patients with metastasis remains poor and undesirable. Notably, 25 % of patients demonstrate metastasis and the target site for metastasis is mainly lung tissue [5]. Accordingly, there is an urgent need for novel drugs to overcome this challenge and improve the prognosis of patients. Among these, bisphosphonates are of interest for treating tumor-induced skeletal diseases owing to their ability to inhibit osteoclast bone resorption and bone metastasis [6]. Zoledronic acid (ZOL) is a next-generation bisphosphonate that is clinically approved for the treatment of metastatic bone disease and substantially affects tumor growth and metastasis [7]. However, recent studies indicates that ZOL has several adverse effects, including renal impairment, which significantly limits its clinical benefits [8,9]. Regarding the potential application of ZOL in osteosarcoma therapy, developing an advanced drug delivery system is vital for improving osteosarcoma management.

The complex tumor microenvironment (TME) is another important barrier that restricts the efficacy of conventional osteosarcoma treatment options [10]. An immunosuppressive TME enhances the immune evasion of cancer cells, leading to treatment resistance in patients with osteosarcoma [11]. The TME significantly affects the effectiveness of cancer treatments by providing physiological barriers, such as inadequate vascularization, immunosuppressive cells, and hypoxia, which decrease drug transfer and facilitate tumor development, resistance, and immune evasion. Advancements in nanotechnology, biomedical imaging, and cell-based therapies, such as macrophage regulation and stem cell interventions, offer promising strategies to influence TME-related barriers and enhance targeted drug delivery and antitumor efficacy [12–14]. Thus, remodeling the immunosuppressive TME could improve the combined efficacy of immunotherapy and chemotherapeutic drugs. Consequently, immunotherapy has been introduced for osteosarcoma management [15]. Emerging research has reported that transforming growth factor beta (TGF-β) signaling can impair the antitumor activity of T cells by shaping the tumor structure, thereby reducing the response rate to immunotherapy [16]. Inhibiting the TGF-β pathway is considered the main approach and a prerequisite for improving the efficacy of tumor immunotherapy. Inhibin Subunit Beta A (INHBA), a member of the TGF-β superfamily, is reportedly upregulated in several tumors [17–19]. An experiment demonstrated that INHBA knockdown using RNA interference technology could reverse the malignant progression of osteosarcoma by downregulating TGF-β [20]. Recently, ZOL combined with thymosin α1 (an immunomodulator) was shown to exert a synergistic effect in the treatment of metastatic prostate cancer by enhancing the activity of cytotoxic T cells [21]. Based on these discussions, we speculated that suppression mediated by ZOL plus INHBA knockdown therapy may be a promising strategy, exerting dual inhibitory effects on osteosarcoma cells and modulating the TME. Currently, small interfering RNAs (siRNAs) are effective tools for inducing gene silencing. However, unmodified siRNA molecules have limited practical applications because of their rapid renal excretion, membrane impermeability, and off-target effects. Consequently, nanostructures have been introduced for siRNA delivery [22]. Therefore, a precise design of the delivery system is essential for realizing the potential of siRNA therapy. In the case of co-delivery of siRNA and chemotherapy, significant tumor suppression can be obtained, which is the aim of this study.

Various nanoparticles (NPs) have been developed to deliver chemotherapeutic drugs and have garnered growing interest for the precise treatment of multiple diseases [23–26]. Nano-delivery systems can effectively enhance the accumulation of drugs in tumors and prevent their premature and burst release, thus providing superior advantages for the co-delivery of therapeutic agents [27]. Carbon quantum dots (CQDs) are promising for delivery applications owing to their low toxicity, physicochemical stability, and fluorescent properties [28]. To overcome this problem, biogenic cell membrane “stealth” strategies have been developed, including erythrocyte, cancer cell, and macrophage membranes. This has resulted in the significant application of biomimetic nanostructures for drug delivery [29]. These strategies preserve the specific biological functions of cells, effectively prolong the circulation time of NPs *in vivo*, and enhance drug accumulation in the targeted cells [30]. Macrophage membranes demonstrate favorable therapeutic potential owing to their ability to recognize disease site receptors and avoid phagocytosis by immune cells [31]. Additionally, given that tumor cells possess an increased number of folate receptors (FR), folic acid (FA), as a ligand, facilitates targeted therapy. Therefore, targeted delivery systems based on FA have been introduced and designed [32].Coupling FA to the NP surface could not only improve specificity but also facilitate the penetration of NPs into the cancer cell membrane via FR-mediated endocytosis [33]. Hence, nanostructures based on CQD- and FA-modified macrophage membrane biomimetic coatings may be suitable platforms for drugs and siRNAs to treat osteosarcoma; however, few studies have explored this therapeutic strategy.

Herein, we developed CQD@RM-FA NP as a co-delivery system for ZOL and siINHBA (ZOL-siINHBA@CQD@RM-FA) and explored their potential application as a drug for osteosarcoma management. This developed biomimetic drug could effectively deliver the loaded siRNA and drug to the tumor region, demonstrating considerable efficacy in suppressing osteosarcoma growth and subsequent lung metastasis (Fig. 1).

## 2. Methods

### 2.1. Materials

The following materials and drugs were used to prepare the nano-delivery system and were obtained from Aladdin (Shanghai, China): citric acid (C434173), polyethylenimine (P684693), dimethylformamide (DMF, D112004), folic acid-polyethylene glycol-N-hydroxysuccinimide (FA-PEG-NHS, F163720), and ZOL (Z129382). The siRNA used to suppress INHBA expression was acquired from GenePharm Co., Ltd. (Shanghai, China) with the following sequence: sense, 5′-GGAUAUCAAGUUCAAUCAA-3′; antisense, 5′-UUGAUUGAACUUGAUUAUCC-3′. The main staining reagents and kits, including Hoechst 33258 (C1017), Annexin V-FITC (C1062S), crystal violet staining (C0121), and Hematoxylin and Eosin Staining Kit (C0105S), were obtained from Beyotime (Shanghai, China); reverse transcription kit FastKing gDNA Dispelling RT SuperMix (KR118-02) was obtained from TIANGEN (Beijing, China); and qPCR reaction kit SYBR Green PCR Master Mix (A4004M) was provided by Lifeint (Xiamen, China). Anti-INHBA (ab56057) and anti-GAPDH (ab181602) antibodies were purchased from Abcam (Cambridge, UK).

### 2.2. Cells and animals

Osteosarcoma cell lines (U2OS and 143B) and mouse macrophages (RAW 264.7) were obtained from ProCell (Wuhan, China) and confirmed via short tandem repeat testing. All cells were cultured in conventional DMEM medium (supplemented with 10 % phosphate-buffered saline (PBS) and 1 % penicillin–streptomycin solution) and incubated in a humidified environment at 37 °C under 5 % $CO_2$. Male BALB/c nude mice were obtained from the Experimental Animal Center of of Shengjing Hospital of China Medical University (Liaoning, China). Animal experiments were performed in accordance with the protocols approved by the Ethics Committee of the Shengjing Hospital of China Medical University (Ethics No. 2025PS163K).

### 2.3. CQD synthesis

CQD were synthesized using a hydrothermal method according to established protocols [34]. First, citric acid (1 g, carbon source) and polyethylenimine (0.2 g; modifier) were dissolved in deionized water (20 mL). After 6 h of reaction in a reactor maintained at 160 °C, the mixture was transferred to a tube and centrifuged at 9000 rpm for 15 min to eliminate the large particles. Subsequently, the solution was

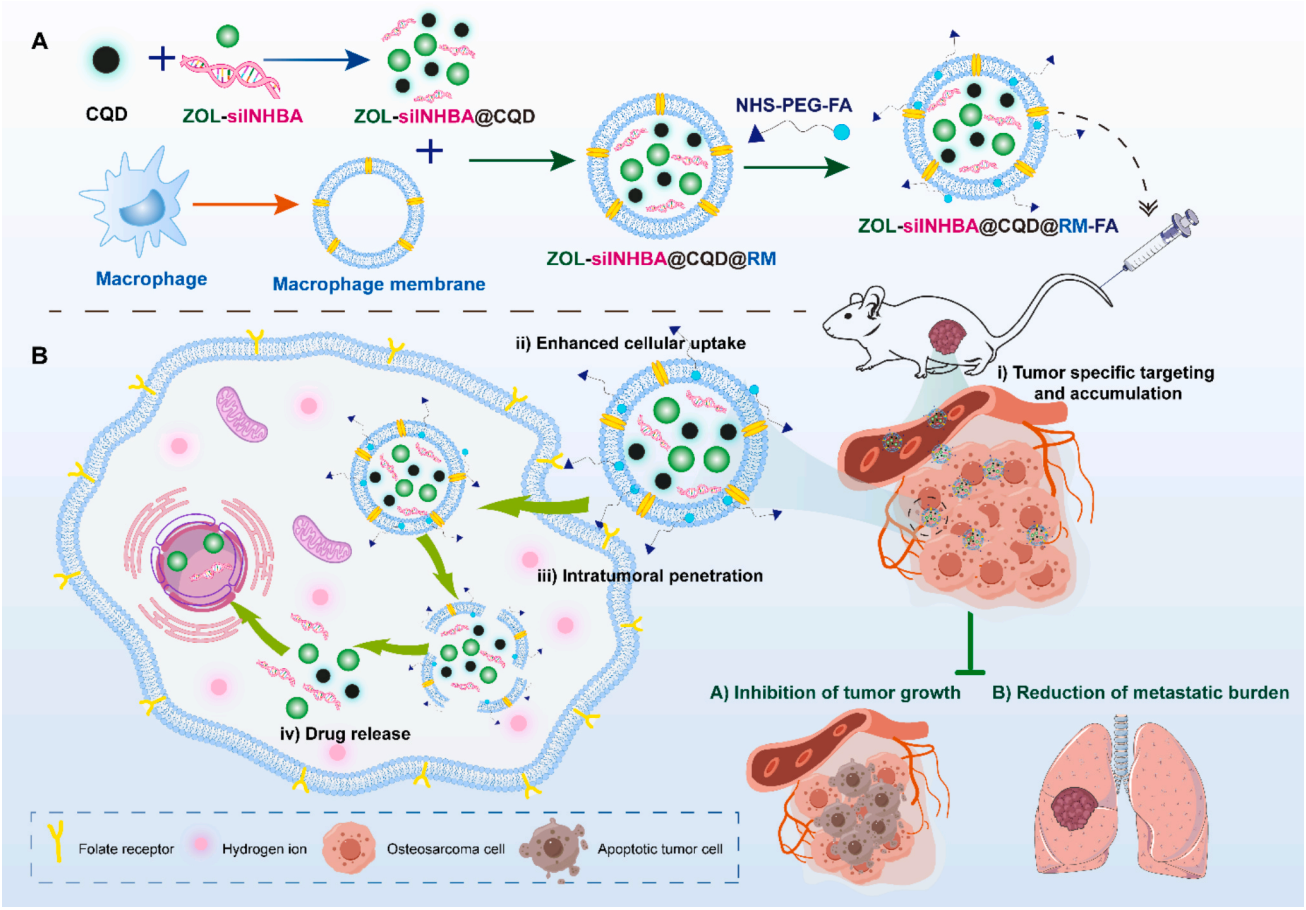


**Fig. 1.** Schematic illustration of the formulation and mechanism of action of ZOL-siINHBA@CQD@RM-FA. (A) CQD nanomaterials were synthesized using the hydrothermal method with citric acid and polyethylenimine as raw materials. Next, CQD were encapsulated with folic acid-modified macrophage membranes, enabling the co-delivery of the anticancer drug ZOL and INHBA siRNA (named ZOL-siINHBA@CQD@RM-FA) to treat mice with primary or lung metastatic osteosarcoma. (B) Mechanistically, ZOL-siINHBA@CQD@RM-FA precisely targeted tumor cells and underwent internalization by cells. Thereafter, these NPs markedly suppressed the proliferation/invasion of cancer cells by releasing ZOL and silencing INHBA expression, thereby promoting tumor growth regression and suppressing lung metastatic burden without inducing systemic toxicity.

dialyzed for 48 h using a dialysis membrane (10000 pore size) to remove unreacted small particles or ions. Finally, the solution was mixed with ethanol (1:5) and centrifuged at 12000 rpm for 10 min. The precipitate was treated with deionized water to obtain a CQD solution, which was freeze-dried to obtain a powdered sample.

### 2.4. Conjugation of CQD/ZOL/siINHBA nanocomplex

The CQD/ZOL/siINHBA nanocomplex was synthesized in two steps. In the first stage, ZOL was added to CQD and mixed for 24 h. The ZOL@CQD nanocomplex was then dialyzed in ultrapure deionized water for 48 h. In the second stage, the dialyzed nanocomplex was mixed with siINHBA for 30 min to obtain ZOL-siINHBA@CQDs.

### 2.5. Isolation of the macrophage cell membrane

Macrophage cell membranes were prepared according to another method [35]. Briefly, RAW 264.7 cells were collected upon reaching 80–90 % confluency and digested with trypsin to obtain a cell suspension. Subsequently, the macrophage suspension was centrifuged at 2000 rpm for 5 min to collect the precipitate. The resulting pellet was dispersed in PBS (pH 7.4) and sonicated in an ice bath for 20 min. The solution was centrifuged at 5000 rpm for 15 min, and the supernatant was collected and sonicated for 10 min to isolate the macrophage membranes (RAW-M).

### 2.6. Preparation of membrane-coated nanocomplexes and modification with FA

Macrophage membrane-coated siINHBA@CQD was prepared using an ultrasonic method. First, ZOL-siINHBA@CQD nanocomplexes were sonicated in an ice bath for 10 min to obtain a dispersion. Next, the sample was mixed with the RAW-M suspension at a mass ratio of 1:70, and 3 mL PBS (pH 7.4) was added. After shaking for 12 h, the mixture was sonicated with 1 mL of PBS for 5 min to form ZOL-siINHBA@CQD@RM. Subsequently, FA-PEG-NHS molecules were dissolved in dimethyl sulfoxide and combined with ZOL-siINHBA@CQD@RM to form the final product, ZOL-siINHBA@CQD@RM-FA.

### 2.7. NP characterization

The characteristics of the generated nanocomplexes were comprehensively determined using the following different methods. First, the nanocomplex micromorphology was characterized using transmission electron microscopy (TEM), and dynamic light scattering was performed to determine the particle size distribution and zeta potential. Second, the samples were scanned using a Fourier transform infrared (FTIR) spectrophotometer to assess the presence of polymers in the nanocomplexes. Third, X-ray diffraction (XRD) and X-ray photoelectron spectroscopy (XPS) analyses were performed using a D8 ADVANCE X-ray

diffractometer to reveal the crystalline nature and surface elemental composition of the nanomaterials.

### 2.8. Determination of drug loading and in vitro drug release capacities

The drug-loading efficiency (DLE) of the ZOL-loaded nanocarriers was measured using ultraviolet (UV) spectrophotometry. A standard curve of the ZOL solution in the concentration range of 0–8 mg/mL was constructed. The 10 mg/mL mother liquor of ZOL was diluted to six solution concentrations: 0, 0.5, 1, 2, 4, and 8 mg/mL. The absorbance values of ZOL-siINHBA@CQD, ZOL-siINHBA@CQD@RM, and ZOL-siINHBA@CQD@RM-FA at 480 nm were measured and compared with those of the standard curve. The DLE was determined using the following formula: DLE (%) = $(W_{loaded\ drug} - W_{feeding\ drug})/W_{loaded\ drug} \times 100$.

In addition, *in vitro* release experiments were conducted to evaluate the effect of the acidic TME on drug release profiles. The release of ZOL and siINHBA from ZOL-siINHBA@CQD@RM-FA within 24 h was determined using the dialysis method, as previously described [36]. Briefly, ZOL-siINHBA@CQD@RM-FA samples were dispersed in dialysis bags containing PBS (2 mL) at pH 5.0, 6.5, or 7.4. Subsequently, the sealed dialysis bags (cut-off 2000 kDa) were immersed in bottles containing PBS (20 mL) at 37 °C in the dark. Samples were collected at specified time points, and the concentration of released ZOL was analyzed using a microplate reader. The release efficiency of 6-carboxyfluorescein (FAM)-labeled siINHBA was quantified by measuring the fluorescence intensity at 488 nm using a microplate spectrophotometer. Based on the standard curve, the release rates (m) of ZOL and siRNA were evaluated using the formula m = A/B, where A is the concentration of ZOL-siRNA in PBS, and B is the initial concentration of ZOL/siRNA loaded in the NP.

### 2.9. Cellular uptake assays

Confocal laser scanning microscopy (CLSM) and flow cytometry were performed to examine the cellular uptake and targeting properties of ZOL-siINHBA@CQD. Osteosarcoma cell lines (U2OS and 143B) were seeded into confocal culture dishes at a density of $1 \times 10^5$ cells/well. The cells were maintained in FITC-labeled ZOL-siINHBA@CQD, ZOL-siINHBA@CQD@RM, ZOL-siINHBA@CQD@RM-FA, or free ZOL + siINHBA DMEM medium at 37 °C/5 % $CO_2$ atmosphere for 2, 4, 8, and 12 h, respectively. FITC was labeled with siINHBA. After removing the medium, the cells were washed with PBS and fixed in a 4 % paraformaldehyde solution, followed by staining of the nuclei using Hoechst for 10 min. Fluorescence images were captured using a fluorescence microscope. Cells from parallel samples were digested with trypsin and resuspended in PBS, followed by flow cytometry analysis of NP uptake.

### 2.10. Reverse transcription and real-time quantitative PCR (RT-qPCR)

Total RNA was extracted from osteosarcoma cell lines or tumor tissues using TRIzol reagent and reverse transcribed into complementary DNA using FastKing RT SuperMix. Subsequently, RT-qPCR was performed using the qPCR SYBR Green Master Mix kit and a real-time fluorescent quantitative PCR system to evaluate INHBA expression in the samples. Gene expression was measured using the $2^{-\Delta\Delta Ct}$ method, with GAPDH as the internal reference. All primer sequences are listed in Table 1.

**Table 1**
Sequences of PCR primers (5′–3′).

| Gene | Forward | Reverse |
|---|---|---|
| Human INHBA | GGAGCTCAGACAGCTCTTACC | ATCTCCGAGGTCTGCTCCAT |
| Human GAPDH | CCATGGGGAAGGTGAAGGTC | AGTGATGGCATGGACTGTGG |
| Mouse INHBA | AAATCAGAACGCCTCCGCTA | TCCAGGGATCACTCCCGAAT |
| Mouse GAPDH | GGCAAATTCAACGGCACAGT | TGAAGTCGCAGGAGACAACC |

### 2.11. Western blotting analysis

The cell lines from each group were lysed with RIPA buffer for 5 min to collect the total protein solution. After performing the bicinchoninic acid assay for protein quantitation, the protein samples (25 μg) were loaded onto sodium dodecyl sulfate–polyacrylamide gel electrophoresis gels for electrophoretic separation and then transferred to polyvinylidene difluoride membranes at 65 V for 2 h. Blots were blocked using 5 % milk for 2 h, followed by sequential incubation with INHBA primary and secondary antibodies. The membranes were developed using an ECL kit, and the density of the bands was quantified using ImageJ software (National Institutes of Health, Bethesda, MD) with GAPDH normalization.

### 2.12. Assessment of in vitro antitumor efficacy

Cell viability was determined using the CCK-8 assay. Exponentially growing U2OS and 143B cells (2000 cells/well) were inoculated into 96-well plates containing 100 μL of complete culture medium and incubated overnight. Subsequently, the medium was replaced with fresh medium containing NPs or free drugs (ZOL and siINHBA). During this period, the final ZOL and siINHBA concentrations were maintained at 20 μM and 0.2 μM, respectively. PBS-treated cells were used as blank controls. All cells were placed in an incubator maintained at 37 °C and 5 % $CO_2$. After 24, 48, and 72 h, respectively, each well was treated with 10 μL of CCK-8 solution for another 2 h. Finally, the absorbance of each well was measured at 450 nm using a microplate reader. In addition, a colony formation assay was performed to evaluate the effects of various NPs on tumor cell proliferative capacity. Briefly, U2OS and 143B cells from different treatment groups were cultured in 6-well plates (400 cells) containing 2 mL of complete medium for 48 h at 37 °C/$CO_2$ for 7 days. Subsequently, the cells were fixed with 1 mL of anhydrous methanol and stained with crystal violet. After washing with PBS, the cells were observed using a fluorescence microscope.

Apoptosis was quantified using an Annexin V-FITC/PI assay. Briefly, U2OS and 143B cells subjected to different treatments were cultured in 6-well plates for 48 h and stained with Annexin V-FITC and PI according to the manufacturer's instructions. Each sample was analyzed by flow cytometry, and the data were analyzed using CELL Quest software.

Furthermore, a Transwell assay was performed to determine the effects of NPs on cell migration and invasion. For the migration analysis, osteosarcoma cells (U2OS and 143B cells, $1 \times 10^6$ cells/well) treated with PBS, NPs, or drugs were inoculated into the Transwell upper chamber. For the invasion analysis, the treated cells were seeded into a Transwell upper chamber pre-coated with Matrigel gel. In both experiments, complete medium (500 μL) with 10 % fetal bovine serum was added to the lower Transwell chamber. Following incubation for 24 h in a 37 °C/$CO_2$ incubator, cotton swabs were used to gently swab the surface of cells that did not migrate or invade. The cells were fixed with formaldehyde, stained with crystal violet, and photographed under an inverted microscope (200 × magnification).

### 2.13. Assessment of in vivo biodistribution

To evaluate the tumor-targeting ability of the NPs, an *in vivo* imaging system was used to assess their biodistribution in an osteosarcoma model. A xenograft model was established by subcutaneously inoculating 143B cells ($1 \times 10^7$ cells/mL) into the right axilla of 5-week-old male BALB/c nude mice. When the tumor grew to a palpable size (approximately 150 mm3), 1 g/kg ZOL + siINHBA, ZOL-siINHBA@CQD, ZOL-siINHBA@CQD@RM, or ZOL-siINHBA@CQD@RM-FA was injected via the tail vein. The final concentrations of ZOL and siINHBA were 5 μg/kg and 5 μM, respectively. After anesthesia induction with 3 % isoflurane at different time points, drug biodistribution in mice was

visualized using an *in vivo* imaging system. Twenty-four hours after drug injection, the mice were anesthetized by administering an intraperitoneal injection of 200 mg/kg sodium pentobarbital and sacrificed, and major organs (heart, liver, spleen, lungs, and kidneys) and tumor tissues were carefully harvested for *ex vivo* imaging.

### 2.14. Assessment of antitumor efficiency in 143B-bearing nude mice

To establish an animal osteosarcoma model, $1 \times 10^7$ 143B cells were subcutaneously inoculated into the right axilla of BALB/c male nude mice (5-week-old). Subsequently, tumor-bearing mice were classified into the following seven groups (n = 6) when the tumor volume reached approximately 150 $mm^3$: PBS, CQD@RM-FA, ZOL, siINHBA, siINHBA@CQD@RM-FA, ZOL@CQD@RM-FA, and ZOL-siINHBA@CQD@RM-FA. The respective agents were injected via the tail vein and administered continuously for 14 days, and tumor weight and volume were monitored continuously. On day 28, blood samples were collected, the mice were sacrificed, and tumor tissues and other organs (heart, liver, and kidneys) were harvested. Blood samples were centrifuged at 5000 rpm for 5 min to separate the serum for biochemical tests. Routine analyses were performed using a fully automated biochemical analyzer to measure the levels of alanine aminotransferase (ALT), aspartate aminotransferase (AST), blood urea nitrogen (BUN), and creatinine (CR), which were used to evaluate liver function. The collected organs and tumor tissues were fixed in 4 % formaldehyde and embedded in paraffin. Tumors and organs were subjected to hematoxylin and eosin (HE) staining, in accordance with standard protocols [3], to evaluate the severity of organ damage. To examine apoptosis, tumor sections were subjected to TUNEL staining using a commercially available kit. Immunohistochemical analysis of the tumor region was performed to determine the expression levels of INHBA. Briefly, after dewaxing and hydration, the sections were subjected to antigen repair and serum blocking procedures. The sections were then incubated overnight with an INHBA-specific primary antibody, followed by incubation with a secondary antibody for 15 min. After hematoxylin staining for 3 min, the number of INHBA-positive cells was determined using a microscope.

### 2.15. Anti-lung metastasis activity studies

Osteosarcoma has a high tendency to metastasize, and lung metastases account for most of distal metastases [37]. Accordingly, we examined the inhibitory effect of NPs on the metastasis of osteosarcoma cells to the lungs. Briefly, Luciferase-labeled 143B cells were injected into the tail vein of the mice to establish a lung metastasis model. After 5 days, PBS, CQD@RM-FA, ZOL, siINHBA, siINHBA@CQD@RM-FA, ZOL@CQD@RM-FA, and ZOL-siINHBA@CQD@RM-FA were administered via the tail vein for 14 days. Lung metastasis was assessed using an *in vivo* imaging system. The mice were sacrificed after the final treatment. Lung tissues were harvested, and luminescence intensity was measured. Tumor nodules formed on the lung surface were visually examined and counted. Lung tissues were embedded in paraffin and stained with HE to examine pathological changes.

### 2.16. Statistical methods

Each experiment was performed in triplicate, and the mean and standard deviation were calculated for each experiment. Statistical analyses were performed using GraphPad Prism (version 8.0; GraphPad Software, Inc., La Jolla, CA, USA). One-way analysis of variance (ANOVA) was used to compare differences between groups, with $P < 0.05$ deemed statistically significant.

## 3. Results

### 3.1. Formulation and characterization of ZOL-siINHBA@CQD@RM-FA

ZOL-siINHBA@CQD@RM-FA was prepared by performing the following four steps: i) synthesizing CQD using a hydrothermal method, as described previously; ii) loading ZOL and siINHBA on CQD to form ZOL-siINHBA@CQD; iii) extracting RAW-M and coating it onto the surface of ZOL-siINHBA@CQD to obtain ZOL-siINHBA@CQD@RM NPs; and (iv) selecting NHS-PEG-FA cell membrane modification to generate the final product (referred to as ZOL-siINHBA@CQD@RM-FA; Fig. 1). As shown in the TEM image, ZOL-siINHBA@CQD@RM-FA exhibited a regular spherical structure (Fig. 2**A**). The average NP size increased with membrane coating and FA-modification. The size distribution histogram shows that the CQD size was ~6 nm, and the NP size (CQD@RM-FA) increased to 151 nm after CM-FA coating. In addition, the particle size of the final product, ZOL-siINHBA@CQD@RM-FA, was ~200 nm, confirming the successful delivery of the internalized drugs ZOL and siINHBA (Fig. 2**B**). The zeta potential of the final NPs (ZOL-siINHBA@CQD@RM-FA) was −32.3 mV (Fig. 2**C**). The CQD exhibited a broad, amorphous peak in the 2θ range (20°–23°), consistent with the lattice spacing of (002) graphitic carbon, and represents the amorphous character of carbon. ZOL and FA exhibited distinct diffraction peaks, indicating their specific crystal structures. Likewise, the ZOL@CQD@RM-FA nanomaterial exhibited characteristic peaks consistent with those of CQD, ZOL, and FA. However, the intensity of these peaks weakened owing to the encapsulation of the cell membrane (Fig. 2**D**).

According to FITR spectral analysis, the CQD peak at 3345 $cm^{-1}$ corresponded to the $OH/NH_2$ telescopic vibration peak; the two characteristic peaks at 1646 $cm^{-1}$ and 1459 $cm^{-1}$ corresponded to the C═O and C═C telescopic vibrations; the peak at 1155 $cm^{-1}$ corresponded to C–O and N–C telescopic vibrations; and the peak at 546 $cm^{-1}$ corresponded to the N–H deformation vibration. In the FTIR spectra of ZOL, the peaks at 628, 673, 707, 763, 760, and 1457 $cm^{-1}$ were attributed to the stretching vibration of the C–H bond in imidazole rings; the peak at 969 $cm^{-1}$ represented the stretching vibration of the C–C bond; the peaks at 1544, 1575, and 1648 cm-1 corresponded to the vibration of the CH═CH group and C–N bond in the imidazole ring; the peak at 1296 $cm^{-1}$ represented the stretching vibration of alcohol groups; and the peaks at 3165 and 3458 $cm^{-1}$ corresponded to the OH bond vibration in the formation of the ZOL dimer. FTIR spectra of FA revealed that 3400–3200 $cm^{-1}$ was the stretching vibration peak of N–H and O–H; 2888 $cm^{-1}$ was the stretching vibration peak of methyl C–H; 1703–1405 $cm^{-1}$ corresponded to the stretching vibration peaks of C═O of ketone or aldehyde and C═C of the aromatic ring or double bond; 1314 $cm^{-1}$ represented the N–H bending vibration peak; 1102 $cm^{-1}$ was the C–O stretching vibration peak of aromatic aldehyde; and peaks of the *para*-disubstituted benzene rings were observed at 837 $cm^{-1}$. Notably, ZOL@CQD@RM-FA displayed weakened infrared absorption peaks after membrane encapsulation and characteristic absorption peaks of C═O, aromatic rings, and C═C for FA at 1700–1500 $cm^{-1}$, indicating the successful formation of the ZOL@CQD@RM-FA structure (Fig. 2**E**). Moreover, the XPS pattern presented three distinct peaks, corresponding to the C1s peak at 284.5 eV, N1s peak at 399.5 eV, and O1s peak at 531.5 eV, proving that nanomaterial ZOL-siINHBA@CQD contained C, N, and O elements (Fig. 2**F**). These findings confirmed the successful generation of ZOL-siINHBA@CQD@RM-FA nanoparticles.

### 3.2. Cellular uptake of ZOL-siINHBA@CQD@RM-FA by osteosarcoma cells

To determine whether CQD@RM-FA could be used for cancer therapy, we analyzed the biocompatibility of the prepared NPs. The DLE of ZOL in ZOL-siINHBA@CQD@RM-FA was 36.15 %, suggesting that the nanodelivery system had a high drug loading rate (Fig. 3**A**). Moreover,

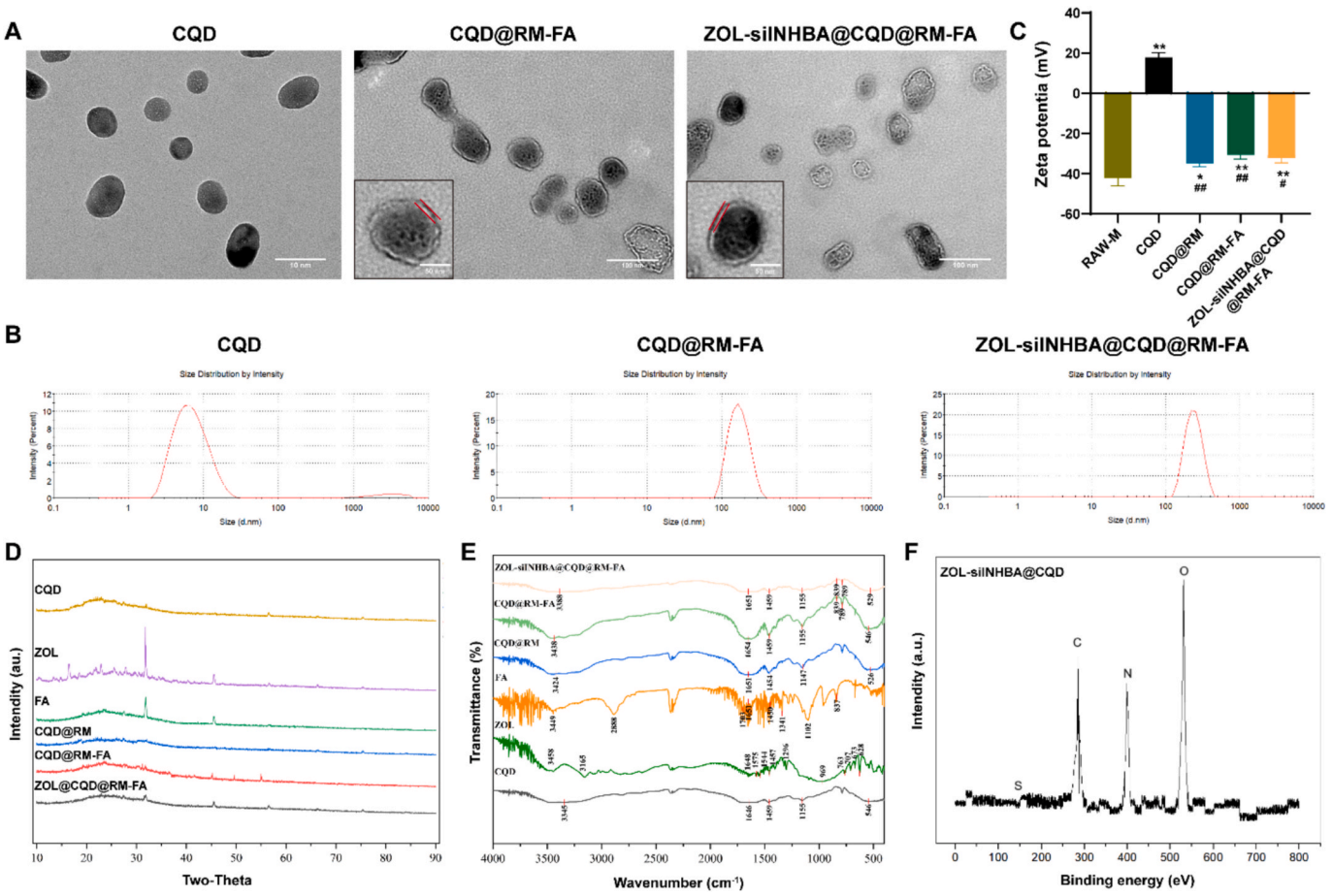


**Fig. 2.** Characterization of NPs for co-delivery of ZOL and siINHBA. (A and B) TEM images and size distribution of CQD, CQD@RM-FA, and ZOL-siINHBA@CQD@RM-FA. (C) Zeta potential. (D and E) XRD pattern and FTIR spectra of CQD, ZOL, FA, CQD@RM, CQD@RM-FA, and ZOL-siINHBA@CQD@RM-FA. (F) XPS spectrum of ZOL-siINHBA@CQD.

we explored the pH sensitivity of ZOL-siINHBA@CQD@RM-FA to verify its pH-triggered drug release ability. At pH 7.4 or 6.5, only small amounts of siINHBA and ZOL (<20 %) were released from ZOL-siINHBA@CQD@RM-FA. However, exposure of NPs to a pH of 5.0 (mimicking the acidic environment of the tumor) resulted in the burst release of drugs, with the cumulative release of ZOL and siINHBA reaching 60 % after 12 h of incubation (Fig. 3**B**). Next, we examined the cellular uptake of NPs by osteosarcoma cell lines (U2OS and 143B) to determine their ability to target cancer cells. In 143B cells, the fluorescence intensity of CQD in the ZOL-siINHBA@CQD@RM-FA group gradually increased as the incubation time increased from 2 to 12 h. Moreover, CLSM images showed that the green fluorescence signal of siRNA and the blue color of the nucleus were highly overlapping in ZOL-siINHBA@CQD@RM-FA-treated cells from 4 h onwards, indicating that the NPs could be efficiently absorbed by tumor cells in a time-dependent manner. Similar results were observed in U2OS cells (Fig. 3**C–E**). Western blotting was performed to characterize the INHBA knockdown efficiency of the nanodelivery system. The CQD@RM-FA complex, including siINHBA@CQD @RM-FA and ZOL-siINHBA@CQD @RM-FA, markedly suppressed INHBA expression in both U2OS and 143B cells (Fig. 3**F**). Therefore, CQD@RM-FA may be an ideal carrier system for the efficient delivery of siRNA and drugs that target tumor cells.

### 3.3. *In vitro anticancer activity of ZOL-siINHBA@CQD@RM-FA in vitro*

RT-qPCR further confirmed the effectiveness of INHBA gene knockdown by NPs. As shown in Fig. 4**A**, in two osteosarcoma cell lines (U2OS and 143B), siINHBA@CQD@RM-FA and ZOL-siINHBA@CQD@RM-FA significantly down-regulated the expression of INHBA gene, compared with other groups. A series of functional experiments was performed to determine the *in vitro* inhibitory effect of ZOL-siINHBA@CQD @RM-FA on osteosarcoma. Herein, we exposed U2OS and 143B cells to PBS, CQD@RM-FA, ZOL, siINHBA, ZOL@CQD@RM-FA, siINHBA@CQD@RM-FA, or ZOL-siINHBA@CQD@RM-FA. CCK8 assay revealed that ZOL-siINHBA@CQD@RM-FA exerted the best inhibitory effect on both U2OS and 143B cells compared with the other treatments (Fig. 4**B**). Colony formation experiments showed that the three drug-loaded CQD@RM-FA nanocarriers effectively reduced osteosarcoma cell (U2OS and 143B) colonization, especially ZOL-siINHBA@CQD@RM-FA (Fig. 4**C and G**). Flow cytometry revealed that ZOL-siINHBA@CQD@RM-FA exhibited the greatest apoptosis-inducing effect in both U2OS and 143B cells compared to the other treatments (Fig. 4**D and G**). In the Transwell assay, ZOL-siINHBA@CQD@RM-FA markedly reduced the invasion and migration of both U2OS and 143B cells (Fig. 4**E–G**). Notably, the cell viability, colony-forming ability, apoptosis, and migration/invasion rates of the ZOL-siINHBA@CQD@RM-FA group were comparable to those of the PBS control group (PBS), suggesting that the nanocarrier materials exerted a minimal impact on cell growth characteristics. Therefore, the simultaneous delivery of ZOL and siINHBA via CQD-RM-FA nanocarriers suppressed tumor progression.

### 3.4. *Biodistribution and antitumor activity of ZOL-siINHBA@CQD@RM-FA in 143B-bearing nude mice*

To visualize the tumor tropism and biodistribution of the

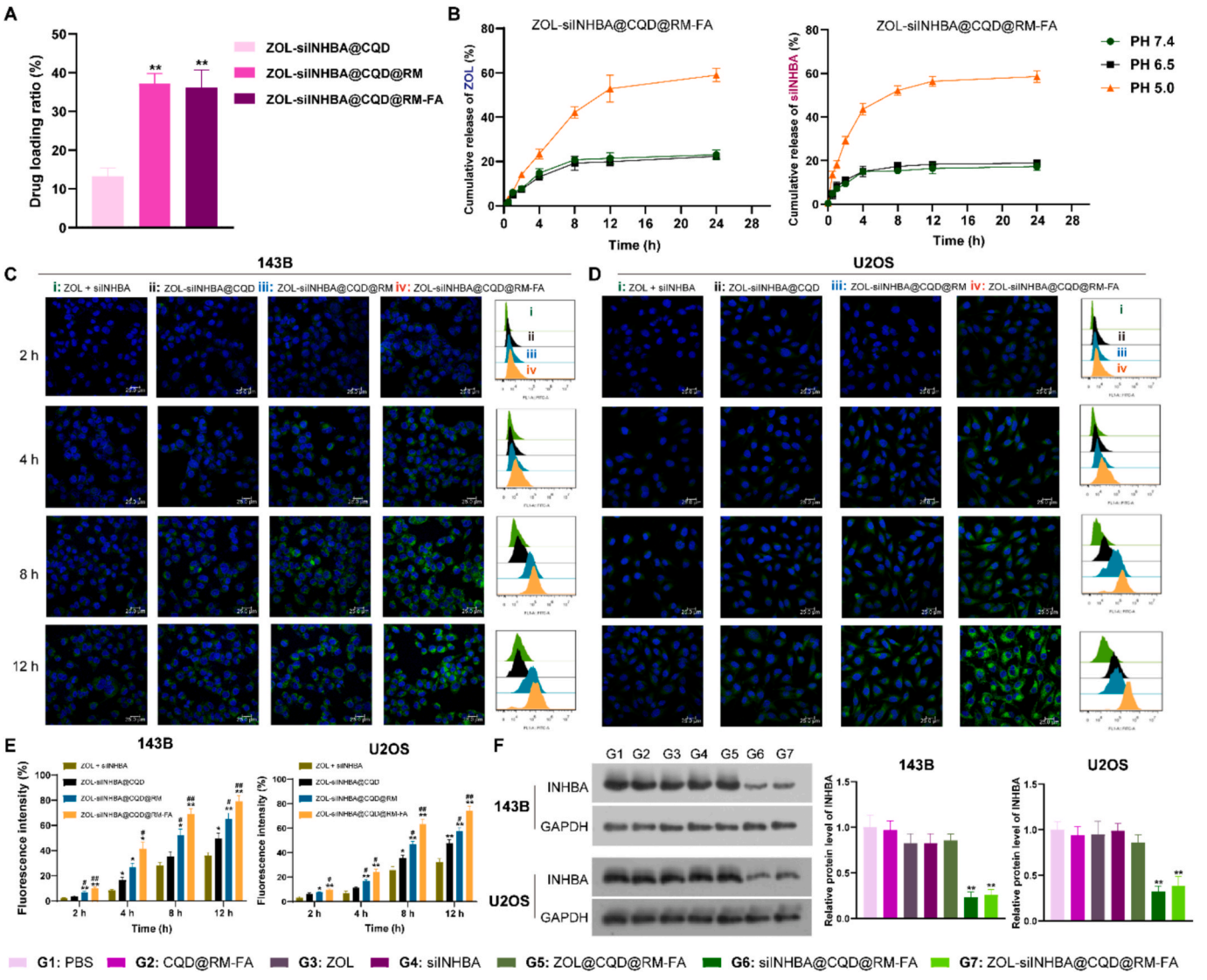


**Fig. 3.** Cellular uptake and pH-responsive performance of NPs. (A) Drug-loading ratios of the different NPs. ** $P < 0.01$ vs. ZOL-siINHBA@CQD. (B) *In vitro* release of ZOL and siINHBA from ZOL-siINHBA@CQD@RM-FA at various pH values. (C, D, and E) Representative confocal images and flow cytometry showing the internalization of free ZOL + siINHBA and different NPs by osteosarcoma cells (U2OS and 143B) after 2, 4, 8, and 12 h of incubation. Green fluorescence represents FITC-labeled siINHBA, and blue fluorescence indicates nuclei stained with DAPI. Scale bar, 25 μm. (F) Western blot analysis of INHBA expression in osteosarcoma cells treated with PBS, CQD@RM-FA, ZOL, siINHBA, ZOL@CQD@RM-FA, siINHBA@CQD@RM-FA, and ZOL-siINHBA@CQD@RM-FA. All data are represented as mean ± SD, N = 3; ** $P < 0.01$ vs. PBS [G1]. (For interpretation of the references to color in this figure legend, the reader is referred to the web version of this article.)

nanomedicine formulation, the fluorescence intensity of each group was monitored using an *in vivo* imaging system (Fig. 5**A**). As shown in Fig. 5**B**, following injection, notable fluorescence signals were detected in the subcutaneous tumor regions of the ZOL-siINHBA@CQD, ZOL-siINHBA@CQD@RM, and ZOL-siINHBA@CQD@RM-FA groups, particularly in the ZOL-siINHBA@CQD@RM-FA. However, the weakest fluorescence signal was detected in mice treated with the free drugs. This finding indicates that FA-modified macrophage membranes enhance the aggregation of ZOL-siINHBA@CQD in tumors. In addition, the fluorescence intensity of the drug steadily increased in the three nanoparticle groups, reaching a peak within the first 9 h, followed by a gradual decay due to metabolism. Notably, the ZOL-siINHBA@CQD@RM-FA group exhibited a higher fluorescence intensity at 24 h than the other groups, indicating its favorable tumor accumulation capacity. We also collected major organs and analyzed them using bioluminescence imaging 24 h post-injection. Fluorescence was detected mainly in the liver, kidneys, and tumor sites of the mice.

To evaluate the *in vivo* antitumor effects of the nanomedicine formulations, 143B-bearing mice were intravenously injected with PBS, CQD@RM-FA, ZOL, siINHBA, ZOL@CQD@RM-FA, siINHBA@CQD@RM-FA, or ZOL-siINHBA@CQD@RM-FA. As shown in Fig. 5**C**, the ZOL-siINHBA@CQD@RM-FA group exhibited the lowest tumor growth rate. The tumor size induced by CQD@RM-FA was comparable to that induced by PBS treatment. Quantification of tumor weight and volume further supported the therapeutic advantages of ZOL-siINHBA@CQD@RM-FA (Fig. 5**D**). Except for free ZOL, the different treatments did not significantly alter the body weights of the mice (Fig. 5**E**). This finding indicates that the formulated nanostructures did not induce notable systemic toxicity in mice. The biosafety of these drugs was assessed *in vivo* using routine blood analysis. Treatment with free ZOL caused notable pathological damage to the liver tissue, as evidenced by the dramatically elevated levels of BUN, ALT, AST, and CR compared to those of the other groups (Fig. 6**A**). Histological evaluation of each group was performed using HE and TUNEL staining. HE staining revealed that the three nanomedicine groups had similar distribution patterns and cell densities in the lungs, liver, spleen, kidneys, and heart,

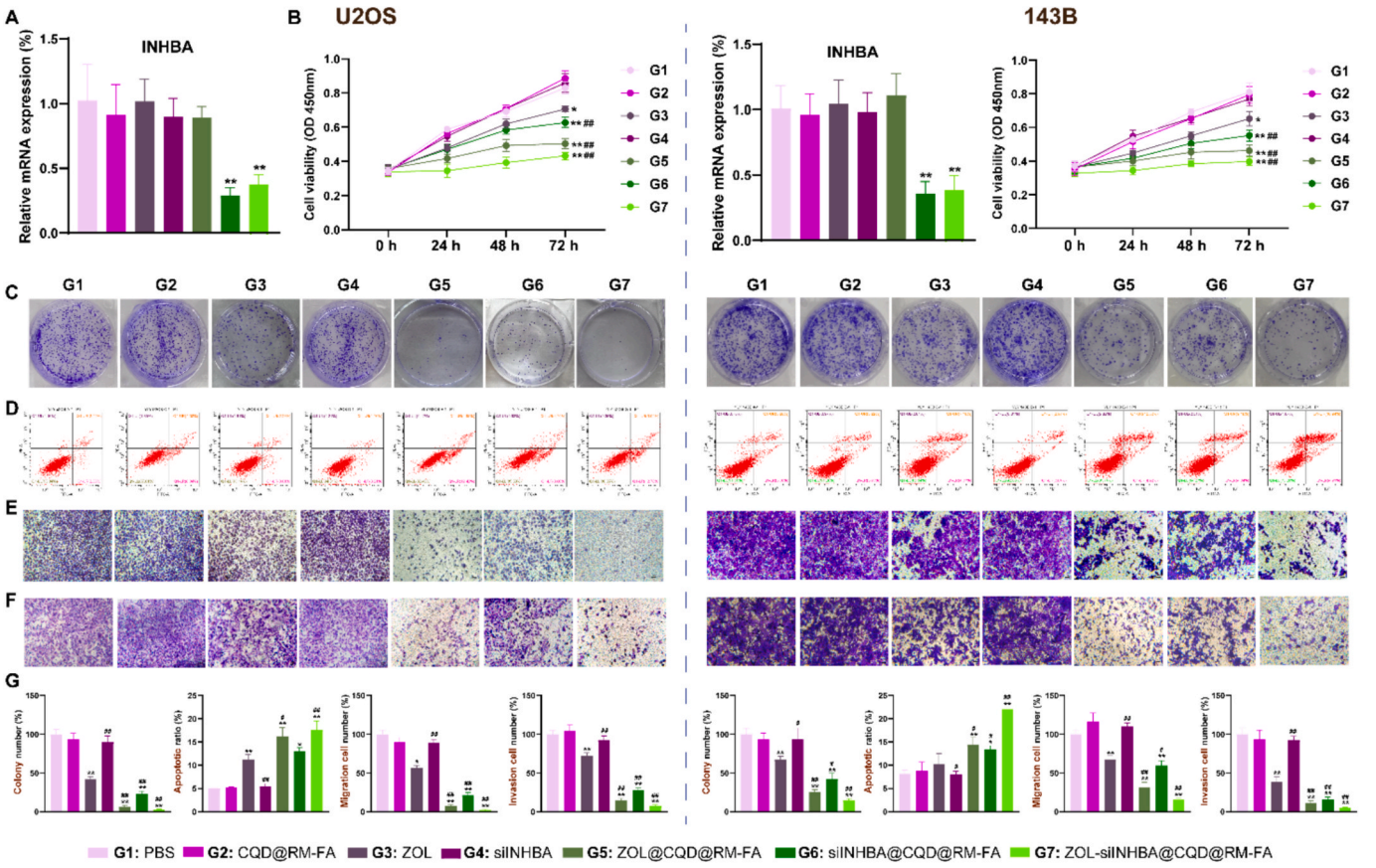


**Fig. 4.** Evaluation of the *in vitro* antitumor properties of different NPs. (A) RT-qPCR assessing the relative mRNA level of INHBA in U2OS or 143B cells treated with different formulations. (B) Viability of U2OS or 143B cells treated with PBS, CQD@RM-FA, ZOL, siINHBA, ZOL@CQD@RM-FA, siINHBA@CQD@RM-FA, and ZOL-siINHBA@CQD@RM-FA. (C) Colony formation in U2OS and 143B cells treated with different formulations. (D) Flow cytometric detection of apoptosis in U2OS and 143B cells treated with different formulations. The cells were stained with Annexin V-FITC. (E and F) Transwell assay for assessing the migration and invasion abilities of U2OS and 143B cells treated with different formulations. (G) Statistical results of cell cloning, apoptosis, migration and invasion. All data are represented as the mean ± SD, N = 3; * $P < 0.05$, ** $P < 0.01$ vs. PBS [G1]; # $P < 0.05$, ## $P < 0.01$ vs. ZOL [G3]. Scale bar, 50 μm.

whereas free ZOL markedly altered liver histology, consistent with the results of serum assessment (Fig. 6**B**). Interestingly, the density of tumor cells in the ZOL-siINHBA@CQD@RM-FA group was lower than that in the other groups. Furthermore, the tumor region of the ZOL-siINHBA@CQD@RM-FA group exhibited the strongest TUNEL fluorescence staining, suggesting that ZOL-siINHBA@CQD@RM-FA induced severe apoptosis in the tumor cells (Fig. 6**C and E**). Immunohistochemical analysis revealed that INHBA expression was effectively suppressed in siINHBA@CQD@RM-FA- and ZOL-siINHBA@CQD@RM-FA-treated mice (Fig. 6**D and E**). A similar result was observed using RT-qPCR analysis (Fig. 6**F**). Collectively, these results suggest that the nanomaterial CQD@RM-FA could effectively load ZOL and siINHBA, exhibit notable tumor suppression ability, and reduce off-target toxicity induced by ZOL alone.

### *3.5. Anti-lung-metastatic activity of ZOL-siINHBA@CQD@RM-FA in 143B-bearing nude mice*

Osteosarcoma is an aggressive mesenchymal tumor with a strong tendency for lung metastasis. To verify whether the assembled nanomedicine formulation could inhibit lung metastasis, we established a mouse model of osteosarcoma lung metastasis (Fig. 7**A**). Bioluminescence monitoring revealed that lung luminescence intensity in mice from the ZOL-siINHBA@CQD@RM-FA group was almost absent (Fig. 7**B**), and the luminescence intensity of the isolated lung tissue was consistent with that observed *in vivo*. Moreover, the number of metastatic lung nodules in the ZOL-siINHBA@CQD@RM-FA group was notably reduced compared with that in the other groups (Fig. 7**C and D**). Further analysis of lung tissue using HE staining revealed no significant pathological changes after treatment with ZOL-siINHBA@CQD@RM-FA. Conversely, the lung tissues of mice in the PBS and free siINHBA groups showed tumor metastasis (Fig. 7**E**). These results indicate that ZOL-siINHBA@CQD@RM-FA effectively suppresses tumor metastasis, underscoring its potential application in treating highly metastatic osteosarcoma.

## 4. Discussion

Despite extensive efforts, the survival rates of patients with osteosarcoma remain poor, and novel therapies in this area are required. Currently, the following major challenges exist in cancer therapy: 1) chemotherapeutic agents, as the gold standard of treatment, are poorly accumulated at the tumor site and may cause dose-dependent side effects, and 2) siRNA therapies targeting oncogenes have disadvantages such as poor cellular uptake and rapid degradation. Therefore, combination therapy and the application of siRNA and other delivery systems are importance [38–40]. Thus, innovations in nanoplatforms for drug and gene delivery can open new avenues for the treatment of osteosarcoma.

In this study, ZOL and siINHBA were efficiently loaded onto CQD, and their exteriors were wrapped and rendered invisible to macrophage membranes. In particular, the macrophage membrane layer was protected by FA modification, which further facilitated the specific entry of NPs into cancer cells for targeted tumor therapy. This meticulously

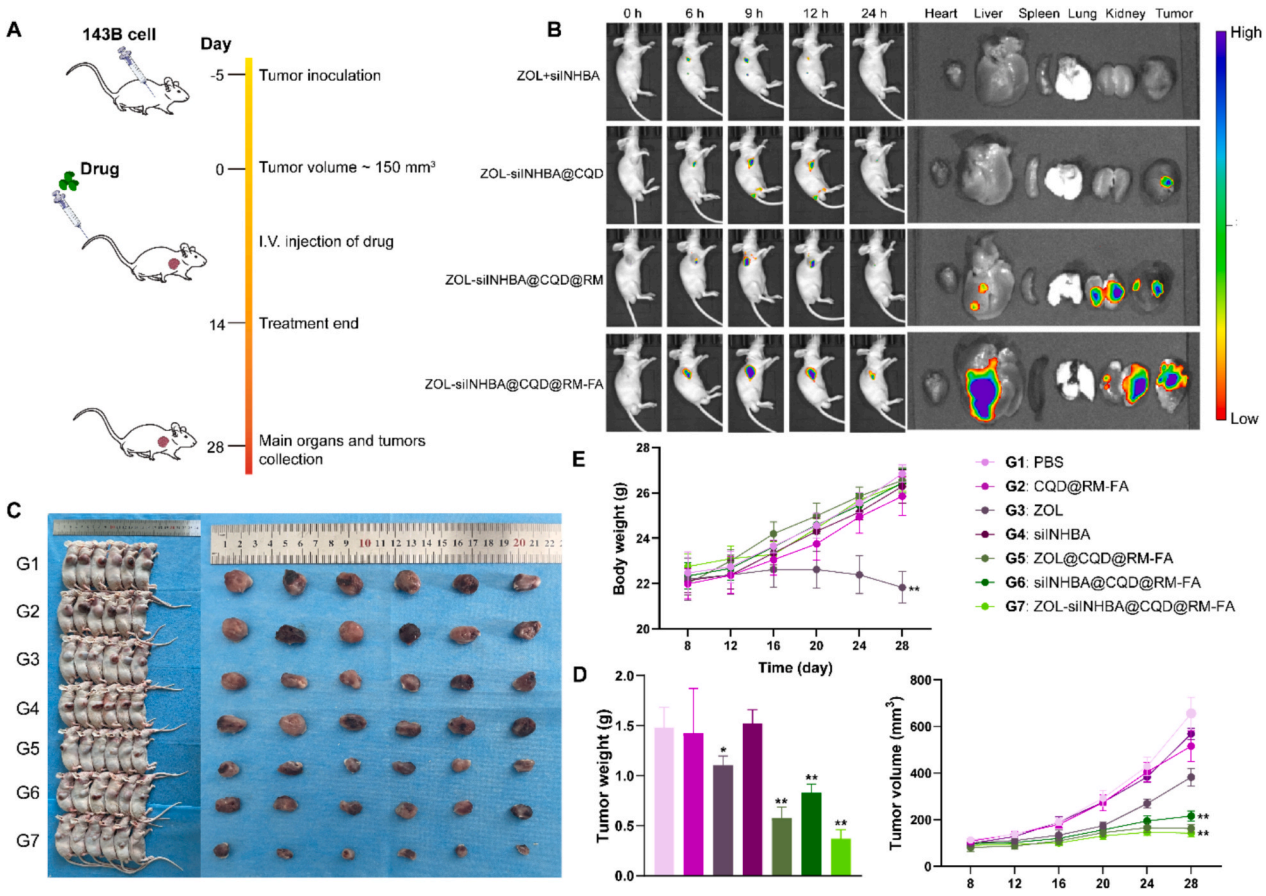


**Fig. 5.** Evaluation of the *in vivo* antitumor efficacy of different NPs in 143B-bearing nude mice. (A) Schematic illustration of the treatment schedule for nanomedicines in 143B xenografts. (B) *In vivo* fluorescence imaging [left] and *ex vivo* imaging [right] of major organs and tumors [right] from 143B tumor-bearing mice 24 h after intravenous administration of free ZOL + siINHBA, ZOL-siINHBA@CQD, ZOL-siINHBA@CQD@RM, or ZOL-siINHBA@CQD@RM-FA. (C) Representative images of the tumors of the 143B tumor-bearing mice treated with PBS, CQD@RM-FA, ZOL, siINHBA, ZOL@CQD@RM-FA, siINHBA@CQD@RM-FA, and ZOL-siINHBA@CQD@RM-FA. (D) Body weights of the tumor-bearing mice. (E) Tumor weights and volumes of tumor-bearing mice. N = 6 in each group; mean ± SD; * $P < 0.05$, ** $P < 0.01$ vs. PBS [G1].

designed nanoplatform can be adapted to complex TMEs owing to the excellent properties of its materials. CQDs are extensively deployed in nanomedicine and can positively contribute to drug delivery with low toxicity and high biocompatibility [41]. Moreover, CQDs can transfect genes into human cells and provide the advantage of fluorescence labeling [42]. Yu et al. demonstrated the potential of CQD combined with siMRP1/doxorubicin to reverse chemotherapy resistance in lung cancer [43], further supporting the rationale for our selection of this biomaterial. Furthermore, we employed macrophage membrane bionics and FA modification techniques to enhance NP stability, which accelerated the uptake of ZOL and siINHBA by tumor cells and precisely targeted the lesion site. FA has been shown to effectively improve the colloidal dispersion stability, biocompatibility, and targeting tumor cells by NPs. NPs can prevent siRNA degradation in the systemic circulation and reduce potential adverse immune reactions [44]. Characterization revealed a particle size of approximately 200 nm. Reportedly, large NPs (100–200 nm) can more easily penetrate tumor vessels and are not easily cleared by the endothelial reticular system. Hence, the size of nanoparticles is important for evaluating their delivery and clearance [45]. Hence, ZOL-siINHBA@CQD@RM-FA exhibited excellent tumor-targeting ability, which is essential for the remote delivery of ZOL and siINHBA.

We further evaluated the drug release behavior of ZOL-siINHBA@CQD@RM-FA. This nanomedicine was pH-dependent, as demonstrated by the release of only a small amount of ZOL or siINHBA at near-neutral pH (7.4), whereas an acidic pH (5.0) triggered a burst release of the drug, especially within the first 12 h. The metabolism (glycolytic metabolism [46]) of cancer cells reportedly leads to the accumulation of $H^+$ ions, resulting in the acidic properties of the surrounding microenvironment [47]. Thus, the constructed ZOL-siINHBA@CQD@RM-FA exhibited controllable drug release. An acidic TME can interfere with the electrostatic interactions between the drug and CQD, thereby triggering NP dissociation and ultimately initiating drug/gene release. Moreover, we examined whether ZOL-siINHBA@CQD@RM-FA could promote the effective internalization of loaded ZOL/siINHBA. Herein, the intracellular drug fluorescence gradually increased with prolonged incubation of ZOL-siINHBA@CQD@RM-FA and osteosarcoma cells, indicating that the loaded ZOL/siINHBA was effectively internalized by the cells. These findings confirmed the therapeutic efficacy of ZOL-siINHBA@CQD@RM-FA.

Based on these findings, we further evaluated the anti-osteosarcoma activity of ZOL-siINHBA@CQD@RM-FA. In cellular experiments, no obvious cytotoxicity was observed in U2OS or 143B cells treated with CQD@RM-FA nanocarriers, suggesting that the NPs had favorable biocompatibility. ZOL-siINHBA@CQD@RM-FA induced a higher apoptosis rate in osteosarcoma cells than free ZOL or siINHBA, accompanied by decreased proliferation, migration, and invasion. ZOL participates in immune regulation by promoting the function of T cells and enhancing the production of chemokines and pro-inflammatory cytokines in tumor cells, thereby suppressing the proliferation and stemness of cancer cells (lung and thyroid cancers). In addition, ZOL can regulate molecular pathways, such as Wnt and STAT3 [48,49]. Moreover, INHBA

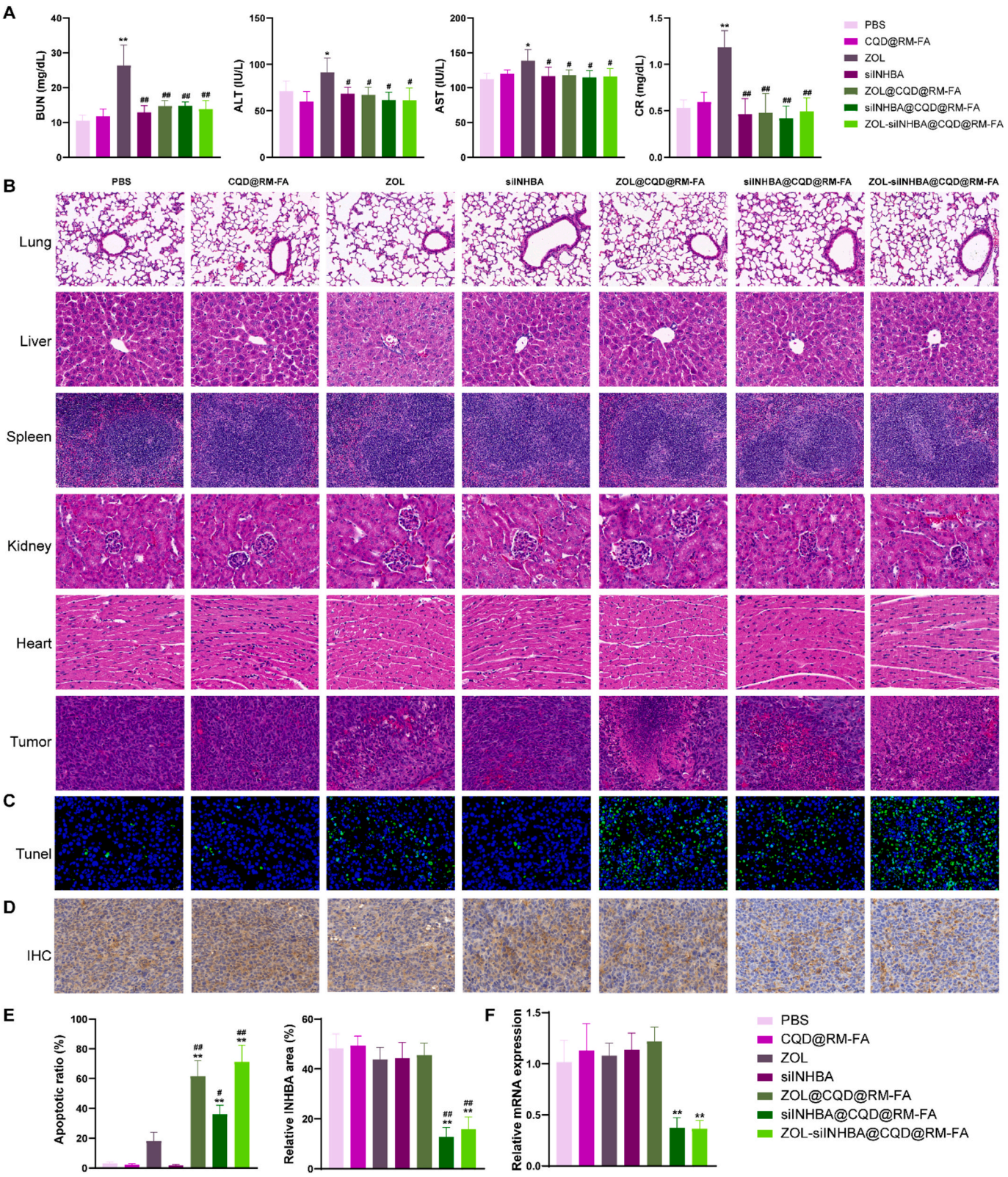


**Fig. 6.** Biosafety assessment of different NPs in 143B-bearing nude mice. (A) Blood biochemical measurements of tumor-bearing mice after injection of PBS, CQD@RM-FA, ZOL, siINHBA, ZOL@CQD@RM-FA, siINHBA@CQD@RM-FA, and ZOL-siINHBA@CQD@RM-FA. (B) Representative HE images of major organs [lung (scale bar, 50 μm), liver (20 μm), spleen (50 μm), kidney (20 μm), heart (20 μm)], and tumor tissues (20 μm) from tumor-bearing mice after treatment with different formulations. (C) TUNEL assay of tumor tissues from mice in each group [scale bar, 20 μm]. (D) Immunohistochemistry assay of INHBA expression in tumor tissues [scale bar, 20 μm]. (E) Quantitative results of the cell apoptosis rate and INHBA expression in tumor tissues. (F) RT-qPCR was used to assess the relative mRNA levels of INHBA in the tumor tissues. N = 6 in each group; mean ± SD; * $P < 0.05$, ** $P < 0.01$ vs. PBS group; # $P < 0.05$, ## $P < 0.01$ vs. ZOL group.

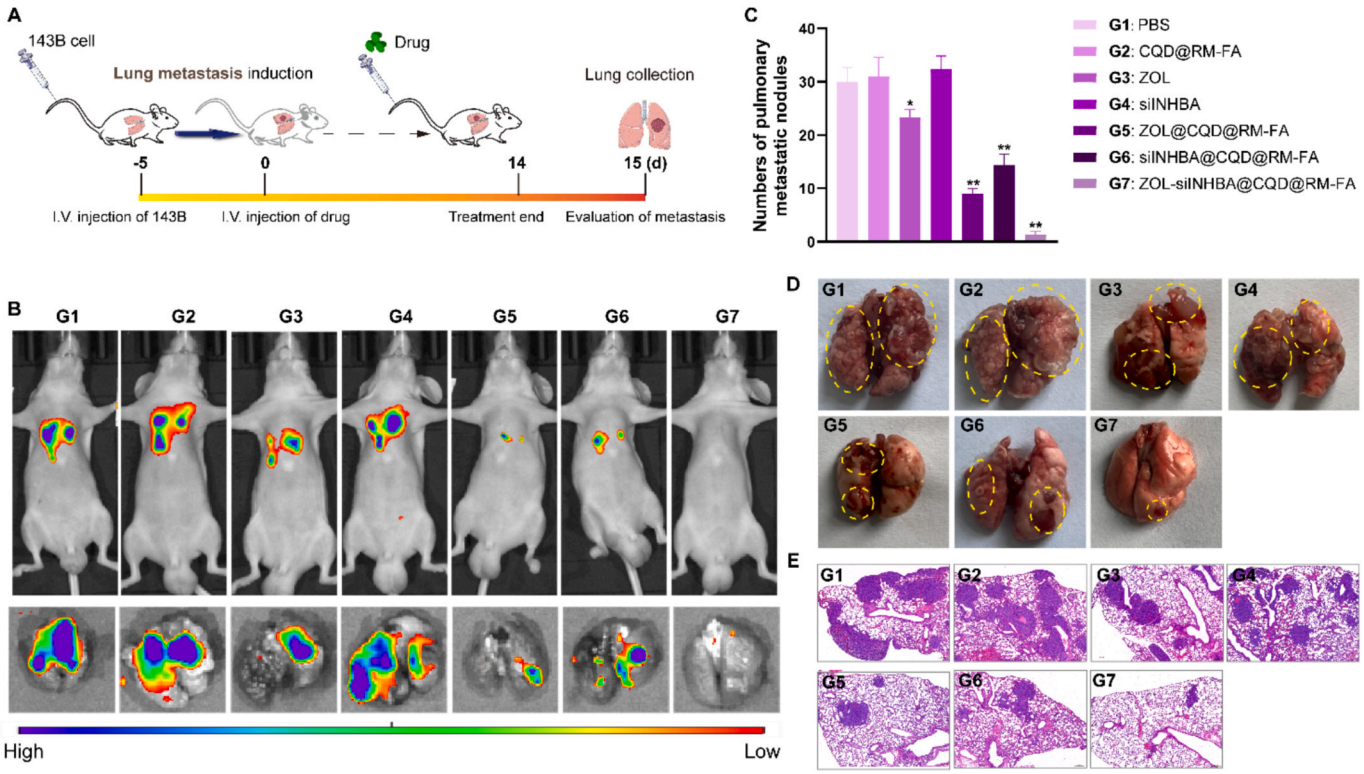


**Fig. 7.** *In vivo* anti-lung metastasis efficacy of different NPs in 143B-bearing nude mice. (A) Schematic illustration of the therapeutic scheme used in the study of lung metastasis. (B) *In vivo* fluorescence imaging [above] and *ex vivo* imaging [below] of lung tissues from 143B tumor-bearing mice 24 h after intravenous administration of PBS, CQD@RM-FA, ZOL, siINHBA, ZOL@CQD@RM-FA, siINHBA@CQD@RM-FA, and ZOL-siINHBA@CQD@RM-FA. (C) Number of pulmonary metastatic nodules after treatment with the different formulations. (D) Representative lung images of mice in each group. (E) Representative H&E-stained images of lung tissues collected from mice that received different treatments. N = 6 in each group; mean ± SD; * $P < 0.05$, ** $P < 0.01$ vs. PBS group.

exerts oncogenic functions, and its deletion reportedly suppresses the growth of several cancers, including lung cell carcinoma and colorectal cancer [50,51]. Therefore, the superior anticancer capacity of the nanomedicine formulation could be attributed to the synergistic effect of ZOL and siRNA, especially the nanosystem, which enhances drug internalization into the cells. In animal experiments, we initially tracked the tissue distribution of ZOL-siINHBA NPs in 143B tumor-bearing mice using fluorescence imaging. ZOL-siINHBA@CQD accurately and selectively reached the tumor site, facilitated by FA-modified macrophage membranes, and remained in the tumor for a longer duration than free drugs. In addition, *in vitro* fluorescence imaging revealed that normal liver clearance caused the fluorescence of the nanomedicine to accumulate in the kidney and liver tissues, ensuring drug biodegradation. Nevertheless, ZOL-siINHBA@CQD@RM-FA ensured the tumor-specific accumulation of drugs. This phenomenon has also been observed in other membrane-modified NPs [52,53]. These results confirmed the high tumor permeability of ZOL-siINHBA@CQD@RM-FA complex. Next, we examined the *in vivo* efficacy of the nanomedicine formulation. ZOL-siINHBA@CQD@RM-FA displayed desirable suppression of osteosarcoma growth and lung metastasis. More importantly, ZOL-siINHBA@CQD@RM-FA exhibited biosafety, with no notable effects on the body weight of mice and significantly reduced free ZOL-induced liver tissue damage.

To design the NPs, we considered macrophage membrane encapsulation, which can easily enable the active targeting of tumor tissues and avoid clearance by the immune system while maintaining systemic circulation. This strategy can induce tumor cell death by modulating the tumor immune microenvironment. For example, Huang et al. designed macrophage membrane-encapsulated nanovesicles (pMETTL14 + RS09) @cRGD-M to achieve the dual purpose of tumor suppression and TME remodeling by precisely targeting tumor cells and inducing macrophage M1 polarization [54]. Moreover, Chen et al. found that macrophage membrane-coated M1/PLGA @IR780/CAT NPs combined with sonodynamic therapy can stimulate T cells and induce the conversion of the TME into an immune-promoting environment, thus effectively decreasing the progression and distal metastasis of breast cancer [55]. In general, nanodelivery systems and functionalized macrophage membranes have promising applications for enhancing the efficacy of immunotherapy and cancer suppression [13,56]. Nevertheless, the current study failed to elucidate the mechanism underlying ZOL-siINHBA@CQD@RM-FA NP-mediated regulation of the TME, which will be the focus of future studies.

In the current study, we designed biomimetic nanomedicine formulations that successfully targeted tumors in preclinical studies, providing significant promise for the precise treatment of osteosarcoma. However, other critical issues must be addressed in future studies. First, despite the low toxicity of ZOL-siINHBA@CQD@RM-FA *in vivo*, considerable effort is still required to optimize the composition, administration dose, and route of NP administration to further improve their long-term therapeutic effect. Second, we only compared the efficacy of NPs with that of ZOL. It remains unclear whether ZOL-siINHBA@CQD@RM-FA retains satisfactory therapeutic potential compared to existing standard osteosarcoma therapies, such as doxorubicin or cisplatin. Third, our understanding of the molecular mechanism of ZOL-siINHBA@CQD@RM-FA affecting the remodeling of TME is limited, and in-depth studies of TME changes will help to improve the clinical outcomes of immunotherapy. Fourth, it focuses on the challenges facing the clinical translation of nanomedicines. On the one hand, the biocompatibility and safety of NPs require to be optimized to ensure their desirable performance *in vivo*. However, efforts are required to reduce research and development costs and strengthen communication with regulatory experts to drive nanomedicines smoothly towards clinical application [57]. In addition,

nanocarriers can be utilized for phototherapy [58,59], and future studies can focus on adding phototherapy to our designed nanostructures to augment cancer therapy. In future studies, we plan to address these issues to facilitate the clinical application of ZOL-siINHBA@CQD@RM-FA.

Another important aspect is the immunological function of the ZOL-siINHBA@CQD@RM-FA nanoplatform. Despite their direct anti-cancer functions, the co-delivery of ZOL and siINHBA can cause TME remodeling by affecting the infiltration and activation of immune cells. The role of ZOL in the regulation of immune cells has been investigated, and it is possible to increase tumor antigen presentation and enhance anti-cancer immunity, along with enhancing the infiltration of dendritic cells, which can be considered in future studies. As a regulator of the TGF-β axis, silencing INHBA can ameliorate immunosuppression in the TME and further enhance anti-cancer immune response. Hence, it is highly suggested that future studies focus on the immunomodulatory functions of this co-delivery system and provide its synergistic function with immune checkpoint inhibitors or cancer vaccines.

In addition to its application in osteosarcoma treatment, the ZOL-siINHBA@CQD@RM-FA platform could be beneficial for treating other tumor types that exhibit INHBA expression and metastasis. Since INHBA is associated with aggressive behavior and poor prognosis, the current findings can be applied to the treatment of other solid tumors as well. In addition, the impact of this nanoplatform on increasing the response of cancer cells to chemotherapy should be evaluated. Future studies should also highlight the biodistribution and therapeutic efficacy of ZOL-siINHBA@CQD@RM-FA in models of other cancers, further demonstrating and validating the versatility and translational potential of this system in multiple tumor types.

## 5. Conclusions

We prepared FA-modified macrophage membrane-coated CQD NPs to ensure the efficient delivery of ZOL and siINHBA into osteosarcoma cells. ZOL-siINHBA@CQD@RM-FA had a suitable particle size and zeta potential, high encapsulation rate, good pH sensitivity, and biocompatibility. Moreover, FA-modified macrophage membranes enhanced the tumor targeting and permeability of the NPs. *In vitro* and *in vivo* assessments revealed that ZOL-siINHBA@CQD@RM-FA achieved desirable therapeutic efficacy by reducing the primary tumor burden and preventing lung metastases. Overall, ZOL-siINHBA@CQD@RM-FA provides a feasible strategy for eliciting improved therapeutic effects in osteosarcoma, which could be extended to different tumor types exhibiting high INHBA expression.

## CRediT authorship contribution statement

**Enyang Yao:** Writing – review & editing, Writing – original draft, Methodology, Investigation. **Yang Li:** Writing – review & editing, Writing – original draft, Methodology, Investigation. **Kai Deng:** Writing – review & editing, Writing – original draft, Methodology, Investigation. **Wei He:** Writing – review & editing, Writing – original draft, Methodology, Investigation. **Milad Ashrafizadeh:** Writing – review & editing, Writing – original draft, Validation, Methodology, Investigation, Conceptualization. **João Conde:** Writing – review & editing, Writing – original draft, Conceptualization. **Liyu Yang:** Writing – review & editing, Writing – original draft, Validation, Supervision, Conceptualization.

## Declaration of competing interest

The authors declare the following financial interests/personal relationships which may be considered as potential competing interests: J. Conde is co-founder and shareholder of TargTex S. A. Targeted therapeutics for Glioblastoma Multiforme. J. Conde is a member of the Global Burden Disease (GBD) consortium from Institute for Health Metrics and Evaluation (IHME), University of Washington (US). The other authors have no competing interests.

## Acknowledgement

L.Y. thanks for the support of Liaoning Province Science and Technology Plan Joint Program (Natural Science Foundation-General Project) (2024-MSLH-559). J.C. acknowledges the Fundação Ciência e Tecnologia, IP national support, through UID/04923 - Comprehensive Health Research Centre.

## Data availability

Data will be made available on request.

## References

[1] H.C. Beird, S.S. Bielack, A.M. Flanagan, J. Gill, D. Heymann, K.A. Janeway, J. A. Livingston, R.D. Roberts, S.J. Strauss, R. Gorlick, Osteosarcoma, Nat. Rev. Dis. Primers 8 (1) (2022) 77, https://doi.org/10.1038/s41572-022-00409-y.
[2] M.S. Kim, I.K. Bolia, B. Iglesias, T. Sharf, S.I. Roberts, H. Kang, A.B. Christ, L. R. Menendez, Timing of treatment in osteosarcoma: challenges and perspectives – a scoping review, BMC Cancer 22 (1) (2022) 970, https://doi.org/10.1186/s12885-022-10061-0.
[3] C. Wu, S. Gong, Y. Duan, C. Deng, S. Kallendrusch, L. Berninghausen, G. Osterhoff, N. Schopow, A tumor microenvironment-based prognostic index for osteosarcoma, J. Biomed. Sci. 30 (1) (2023) 23, https://doi.org/10.1186/s12929-023-00917-3.
[4] J. Zhao, D.C. Dean, F.J. Hornicek, X. Yu, Z. Duan, Emerging next-generation sequencing-based discoveries for targeted osteosarcoma therapy, Cancer Lett. 474 (2020) 158–167, https://doi.org/10.1016/j.canlet.2020.01.020.
[5] A. Smrke, P.M. Anderson, A. Gulia, S. Gennatas, P.H. Huang, R.L. Jones, Future directions in the treatment of osteosarcoma, Cells 10 (1) (2021) 172, https://doi.org/10.3390/cells10010172.
[6] L. Xing, F.H. Ebetino, R.K. Boeckman, V. Srinivasan, J. Tao, T.K. Sawyer, J. Li, Z. Yao, B.F. Boyce, Targeting anti-cancer agents to bone using bisphosphonates, Bone 138 (2020) 115492, https://doi.org/10.1016/j.bone.2020.115492.
[7] L. Wang, D. Fang, J. Xu, R. Luo, Various pathways of zoledronic acid against osteoclasts and bone cancer metastasis: a brief review, BMC Cancer 20 (1) (2020) 1059, https://doi.org/10.1186/s12885-020-07568-9.
[8] S. Li, P. Chen, Y. Pei, K. Zheng, W. Wang, E. Qiu, X. Zhang, Addition of zoledronate to chemotherapy in patients with osteosarcoma treated with limb-sparing surgery: a phase III clinical trial, Med. Sci. Monit. 25 (2019) 1429–1438, https://doi.org/10.12659/MSM.913236.
[9] A. Christou, N. Ferreira, A. Sophocleous, Effects of zoledronic acid on osteosarcoma progression and metastasis: systematic review and meta-analysis, Clin. Exp. Med. 23 (7) (2023) 3041–3051, https://doi.org/10.1007/s10238-022-00961-7.
[10] I. Corre, F. Verrecchia, V. Crenn, F. Redini, V. Trichet, The osteosarcoma microenvironment: a complex but targetable ecosystem, Cells 9 (4) (2020) 976, https://doi.org/10.3390/cells9040976.
[11] W. Liu, H. Hu, Z. Shao, X. Lv, Z. Zhang, X. Deng, Q. Song, Y. Han, T. Guo, L. Xiong, B. Wang, Y. Zhang, Characterizing the tumor microenvironment at the single-cell level reveals a novel immune evasion mechanism in osteosarcoma, Bone Res. 11 (1) (2023) 4, https://doi.org/10.1038/s41413-022-00237-6.
[12] Y.Q. Cheng, S.B. Wang, J.H. Liu, L. Jin, Y. Liu, C.Y. Li, Y.R. Su, Y.R. Liu, X. Sang, Q. Wan, C. Liu, L. Yang, Z.C. Wang, Modifying the tumour microenvironment and reverting tumour cells: new strategies for treating malignant tumours, Cell Prolif. 53 (8) (2020) e12865, https://doi.org/10.1111/cpr.12865.
[13] Y. Zheng, Y. Han, Q. Sun, Z. Li, Harnessing anti-tumor and tumor-tropism functions of macrophages via nanotechnology for tumor immunotherapy, Exploration (Beijing) 2 (3) (2022) 20210166, https://doi.org/10.1002/exp.20210166.
[14] A.S. Moody, P.A. Dayton, W.C. Zamboni, Imaging methods to evaluate tumor microenvironment factors affecting nanoparticle drug delivery and antitumor response, Cancer drug resistance (Alhambra, Calif.) 4(2) (2021) 382-413. https://doi.org/10.20517/cdr.2020.94.
[15] C. Chen, L. Xie, T. Ren, Y. Huang, J. Xu, W. Guo, Immunotherapy for osteosarcoma: fundamental mechanism, rationale, and recent breakthroughs, Cancer Lett. 500 (2021) 1–10, https://doi.org/10.1016/j.canlet.2020.12.024.
[16] R. Derynck, S.J. Turley, R.J. Akhurst, TGFβ biology in cancer progression and immunotherapy, Nat. Rev. Clin. Oncol. 18 (1) (2021) 9–34, https://doi.org/10.1038/s41571-020-0403-1.
[17] M. Okano, H. Yamamoto, H. Ohkuma, Y. Kano, H. Kim, S. Nishikawa, M. Konno, K. Kawamoto, N. Haraguchi, I. Takemasa, T. Mizushima, M. Ikeda, T. Yokobori, K. Mimori, M. Sekimoto, Y. Doki, M. Mori, H. Ishii, Significance of INHBA expression in human colorectal cancer, Oncol. Rep. 30 (6) (2013) 2903–2908, https://doi.org/10.3892/or.2013.2761.
[18] Q. Wang, Y.-G. Wen, D.-P. Li, J. Xia, C.-Z. Zhou, D.-W. Yan, H.-M. Tang, Z.-H. Peng, Upregulated INHBA expression is associated with poor survival in gastric cancer, Med. Oncol. 29 (1) (2012) 77–83, https://doi.org/10.1007/s12032-010-9766-y.
[19] S. Chen, Y. Gong, Y. Shen, Y. Liu, Y. Fu, Y. Dai, A.U. Rehman, L. Tang, H. Liu, INHBA is a novel mediator regulating cellular senescence and immune evasion in colorectal cancer, J. Cancer 12 (19) (2021) 5938–5949, https://doi.org/10.7150/jca.61556.

[20] H. Zhang, Y. Huang, Q. Wen, Y. Li, L. Guo, N. Ge, INHBA gene silencing inhibits proliferation, migration, and invasion of osteosarcoma cells by repressing TGF-β signaling pathway activation, J. Orthop. Surg. Res. 18 (1) (2023) 848, https://doi.org/10.1186/s13018-023-04330-2.
[21] S. Wang, M. Huang, M. Chen, Z. Sun, Y. Jiao, G. Ye, J. Pan, W. Ye, J. Zhao, D. Zhang, Zoledronic acid and thymosin α1 elicit antitumor immunity against prostate cancer by enhancing tumor inflammation and cytotoxic T cells, J. Immunother. Cancer 11 (6) (2023) e006381, https://doi.org/10.1136/jitc-2022-006381.
[22] M. Moazzam, M. Zhang, A. Hussain, X. Yu, J. Huang, Y. Huang, The landscape of nanoparticle-based siRNA delivery and therapeutic development, Mol. Ther. 32 (2) (2024) 284–312, https://doi.org/10.1016/j.ymthe.2024.01.005.
[23] P. Gong, H. Cui, C. Li, S. Song, Y. Gong, J. Li, B. Wang, F. Liu, D. Wang, Z. Liu, Self-stablized monodispersing nano-MOFs for controlled enzyme delivery, Chem. Eng. J. 489 (2024) 150941, https://doi.org/10.1016/j.cej.2024.150941.
[24] P. Gong, M. Wang, J. Wang, J. Li, B. Wang, X. Bai, J. Liu, Z. Liu, D. Wang, W. Liu, A biomimetic lubricating nanosystem for synergistic therapy of osteoarthritis, J. Colloid Interface Sci. 672 (2024) 589–599, https://doi.org/10.1016/j.jcis.2024.06.009.
[25] C. Li, P. Gong, M. Chao, J. Li, L. Yang, Y. Huang, D. Wang, J. Liu, Z. Liu, A Biomimetic lubricating nanosystem with responsive drug release for osteoarthritis synergistic therapy, Adv. Healthc. Mater. 12 (12) (2023) e2203245, https://doi.org/10.1002/adhm.202203245.
[26] D. Wang, J. Li, C. Niu, Y. Wu, S. Gong, Z. Liu, J. Liu, P. Gong, W. Liu, Biomimetic lubricating COFs with donor-acceptor structure for osteoarthritis therapy, J. Colloid Interface Sci. 687 (2025) 85–94, https://doi.org/10.1016/j.jcis.2025.01.238.
[27] B. Xiao, L. Ma, D. Merlin, Nanoparticle-mediated co-delivery of chemotherapeutic agent and siRNA for combination cancer therapy, Expert Opin. Drug Deliv. 14 (1) (2017) 65–73, https://doi.org/10.1080/17425247.2016.1205583.
[28] M.J. Molaei, A review on nanostructured carbon quantum dots and their applications in biotechnology, sensors, and chemiluminescence, Talanta 196 (2019) 456–478, https://doi.org/10.1016/j.talanta.2018.12.042.
[29] B.T. Luk, L. Zhang, Cell membrane-camouflaged nanoparticles for drug delivery, J. Control. Release 220 (Pt B) (2015) 600–607, https://doi.org/10.1016/j.jconrel.2015.07.019.
[30] S. Tan, T. Wu, D. Zhang, Z. Zhang, Cell or cell membrane-based drug delivery systems, Theranostics 5 (8) (2015) 863–881, https://doi.org/10.7150/thno.11852.
[31] Y. Wu, S. Wan, S. Yang, H. Hu, C. Zhang, J. Lai, J. Zhou, W. Chen, X. Tang, J. Luo, X. Zhou, L. Yu, L. Wang, A. Wu, Q. Fan, J. Wu, Macrophage cell membrane-based nanoparticles: a new promising biomimetic platform for targeted delivery and treatment, J. Nanobiotechnol. 20 (1) (2022) 542, https://doi.org/10.1186/s12951-022-01746-6.
[32] J. Sudimack, R.J. Lee, Targeted drug delivery via the folate receptor, Adv. Drug Deliv. Rev. 41 (2) (2000) 147–162, https://doi.org/10.1016/s0169-409x(99)00062-9.
[33] J. Wang, L. Zhang, H. Xin, Y. Guo, B. Zhu, L. Su, S. Wang, J. Zeng, Q. Chen, R. Deng, Z. Wang, J. Wang, X. Jin, S. Gui, Y. Xu, X. Lu, Mitochondria-targeting folic acid-modified nanoplatform based on mesoporous carbon and a bioactive peptide for improved colorectal cancer treatment, Acta Biomater. 152 (2022) 453–472, https://doi.org/10.1016/j.actbio.2022.08.071.
[34] S. Yu, F. Guo, Y. Luo, X. Zhang, C. Wang, Y. Liu, H. Zhang, Electropositive citric acid-polyethyleneimine carbon dots carrying the PINK1 gene regulate ATP-related metabolic dysfunction in APP/PS1-N2a cells, Molecules 29 (9) (2024) 1907, https://doi.org/10.3390/molecules29091907.
[35] P. Ye, L. Li, X. Qi, M. Chi, J. Liu, M. Xie, Macrophage membrane-encapsulated nitrogen-doped carbon quantum dot nanosystem for targeted treatment of Alzheimer's disease: regulating metal ion homeostasis and photothermal removal of β-amyloid, J. Colloid Interface Sci. 650 (Pt B) (2023) 1749–1761, https://doi.org/10.1016/j.jcis.2023.07.132.
[36] T. Ge, Z. Weiwei, F. Ge, L. Zhu, P. Song, W. Li, L. Gui, W. Dong, Y. Tao, K. Yang, A bone-targeting drug delivery vehicle of a metal-organic framework conjugate with zoledronate combined with photothermal therapy for tumor inhibition in cancer bone metastasis, Biomater. Sci. 10 (7) (2022) 1831–1843, https://doi.org/10.1039/d1bm01717a.
[37] H. Mamdani, S.J. Grethlein, Pulmonary metastases from chondroblastic osteosarcoma, N. Engl. J. Med. 378 (15) (2018) 1429, https://doi.org/10.1056/NEJMicm1711874.
[38] D.M. Anwar, M. El-Sayed, A. Reda, J.-Y. Fang, S.N. Khattab, A.O. Elzoghby, Recent advances in herbal combination nanomedicine for cancer: delivery technology and therapeutic outcomes, Expert Opin. Drug Deliv. 18 (11) (2021) 1609–1625, https://doi.org/10.1080/17425247.2021.1955853.
[39] H. Isazadeh, F. Oruji, S. Shabani, J. Behroozi, H. Nasiri, A. Isazadeh, M. Akbari, Advances in siRNA delivery approaches in cancer therapy: challenges and opportunities, Mol. Biol. Rep. 50 (11) (2023) 9529–9543, https://doi.org/10.1007/s11033-023-08749-y.
[40] N. Khelghati, J. Soleimanpour Mokhtarvand, M. Mir, F. Alemi, Z. Asemi, A. Sadeghpour, M. Maleki, H. Samadi Kafil, F. Jadidi-Niaragh, M. Majidinia, B. Yousefi, The importance of co-delivery of nanoparticle-siRNA and anticancer agents in cancer therapy, Chem. Biol. Drug Des. 97 (4) (2021) 997–1015, https://doi.org/10.1111/cbdd.13824.
[41] P. Devi, S. Saini, K.-H. Kim, The advanced role of carbon quantum dots in nanomedical applications, Biosens. Bioelectron. 141 (2019) 111158, https://doi.org/10.1016/j.bios.2019.02.059.
[42] J. Zhou, W. Deng, Y. Wang, X. Cao, J. Chen, Q. Wang, W. Xu, P. Du, Q. Yu, J. Chen, M. Spector, J. Yu, X. Xu, Cationic carbon quantum dots derived from alginate for gene delivery: One-step synthesis and cellular uptake, Acta Biomater. 42 (2016) 209–219, https://doi.org/10.1016/j.actbio.2016.06.021.
[43] H. Yu, K. Tang, Z. Cai, X. Lin, Y. Huang, T. Yu, Q. Zhang, Q. Wang, L. Wu, L. Yang, H. Shan, H. Luo, Carbon dots-based nanozyme for drug-resistant lung cancer therapy by encapsulated doxorubicin/siRNA cocktail, Int. J. Nanomed. 18 (2023) 933–948, https://doi.org/10.2147/IJN.S390984.
[44] K.A. Whitehead, R. Langer, D.G. Anderson, Knocking down barriers: advances in siRNA delivery, Nat. Rev. Drug Discov. 8 (2) (2009) 129–138, https://doi.org/10.1038/nrd2742.
[45] M. Xu, Y. Qi, G. Liu, Y. Song, X. Jiang, B. Du, Size-dependent in vivo transport of nanoparticles: implications for delivery, targeting, and clearance, ACS Nano 17 (21) (2023) 20825–20849, https://doi.org/10.1021/acsnano.3c05853.
[46] X. Li, R. Yue, G. Guan, C. Zhang, Y. Zhou, G. Song, Recent development of pH-responsive theranostic nanoplatforms for magnetic resonance imaging-guided cancer therapy, Exploration (Beijing) 3 (3) (2023) 20220002, https://doi.org/10.1002/exp.20220002.
[47] E. Boedtkjer, S.F. Pedersen, The acidic tumor microenvironment as a driver of cancer, Annu. Rev. Physiol. 82 (2020) 103–126, https://doi.org/10.1146/annurev-physiol-021119-034627.
[48] J. Lv, F.-K. Chen, C. Liu, P.-J. Liu, Z.-P. Feng, L. Jia, Z.-X. Yang, F. Hou, Z.-Y. Deng, Zoledronic acid inhibits thyroid cancer stemness and metastasis by repressing M2-like tumor-associated macrophages induced Wnt/β-catenin pathway, Life Sci. 256 (2020) 117925, https://doi.org/10.1016/j.lfs.2020.117925.
[49] X. Yang, Y. Gao, Q. Liu, L. Wan, H. Liu, W. Bian, Y. Du, C. Huang, Zoledronic acid re-sensitises gefitinib-resistant lung cancer cells by inhibiting the JAK/STAT3 signalling pathway and reversing epithelial-mesenchymal transition, Oncol. Rep. 45 (2) (2021) 459–468, https://doi.org/10.3892/or.2020.7881.
[50] S. Taniguchi, T. Matsui, K. Kimura, S. Funaki, Y. Miyamoto, Y. Uchida, T. Sudo, J. Kikuta, T. Hara, D. Motooka, Y.-C. Liu, D. Okuzaki, E. Morii, N. Emoto, Y. Shintani, M. Ishii, In vivo induction of activin A-producing alveolar macrophages supports the progression of lung cell carcinoma, Nat. Commun. 14 (1) (2023) 143, https://doi.org/10.1038/s41467-022-35701-8.
[51] Q. Xiao, J. Xiao, J. Liu, J. Liu, G. Shu, G. Yin, Metformin suppresses the growth of colorectal cancer by targeting INHBA to inhibit TGF-β/PI3K/AKT signaling transduction, Cell Death Dis. 13 (3) (2022) 202, https://doi.org/10.1038/s41419-022-04649-4.
[52] Z. Cao, X. Liu, W. Zhang, K. Zhang, L. Pan, M. Zhu, H. Qin, C. Zou, W. Wang, C. Zhang, Y. He, W. Lin, Y. Zhang, D. Han, M. Li, J. Gu, Biomimetic macrophage membrane-camouflaged nanoparticles induce ferroptosis by promoting mitochondrial damage in glioblastoma, ACS Nano 17 (23) (2023) 23746–23760, https://doi.org/10.1021/acsnano.3c07555.
[53] K. Ying, Y. Zhu, J. Wan, C. Zhan, Y. Wang, B. Xie, P. Xu, H. Pan, H. Wang, Macrophage membrane-biomimetic adhesive polycaprolactone nanocamptothecin for improving cancer-targeting efficiency and impairing metastasis, Bioact. Mater. 20 (2023) 449–462, https://doi.org/10.1016/j.bioactmat.2022.06.013.
[54] X. Huang, L. Wang, H. Guo, W. Zhang, Macrophage membrane-coated nanovesicles for dual-targeted drug delivery to inhibit tumor and induce macrophage polarization, Bioact. Mater. 23 (2023) 69–79, https://doi.org/10.1016/j.bioactmat.2022.09.027.
[55] S. Chen, T. Ma, J. Wang, S. Liang, H. Liao, W. Tan, M. Chen, X. Zhou, Y. Xu, L. Wang, C. Niu, Macrophage-derived biomimetic nanoparticles enhanced SDT combined with immunotherapy inhibited tumor growth and metastasis, Biomaterials 305 (2024) 122456, https://doi.org/10.1016/j.biomaterials.2023.122456.
[56] X. Huang, W. Zhang, Overcoming T cell exhaustion in tumor microenvironment via immune checkpoint modulation with nano-delivery systems for enhanced immunotherapy, Small Methods 8 (8) (2024) e2301326, https://doi.org/10.1002/smtd.202301326.
[57] P.J. Gawne, M. Ferreira, M. Papaluca, J. Grimm, P. Decuzzi, New opportunities and old challenges in the clinical translation of nanotheranostics, Nat. Rev. Mater. 8 (12) (2023) 783–798, https://doi.org/10.1038/s41578-023-00581-x.
[58] S. Song, D. Wang, K. Zhao, Y. Wu, P. Zhang, J. Liu, G. Yang, P. Gong, Z. Liu, Donor-acceptor structured photothermal COFs for enhanced starvation therapy, Chem. Eng. J. 442 (2022) 135963, https://doi.org/10.1016/j.cej.2022.135963.
[59] P. Gong, C. Li, D. Wang, S. Song, W. Wu, B. Liu, J. Shen, J. Liu, Z. Liu, Enzyme coordination conferring stable monodispersity of diverse metal–organic frameworks for photothermal/starvation therapy, J. Colloid Interface Sci. 642 (2023) 612–622, https://doi.org/10.1016/j.jcis.2023.03.178.